AIAA JOURNAL
Vol. 49, No. 10, October 2011

Damping of Rotating Beams with Particle Dampers: Experimental Analysis

Daniel N. J. Els*
University of Stellenbosch, Matieland 7602, South Africa

DOI: 10.2514/1.J050984

The main objective was to determine the performance of a particle damper under centrifugal loads. A test bench was developed, consisting of a rotating cantilever beam with a particle damper at the tip. Equal mass containers with different depths, filled with a range of uniform-sized steel ball bearings, were used as particle dampers. For all the tests, the total particle damper mass was identical. During operation, the tip of the beam was displaced, and after release the beam could vibrate freely. The decay in the vibratory motion of the tip of the beam was measured over a range of centrifugal loads. It was found that there is a zone with a high- and one with a low-damping factor. These zones depend on the ratio between the peak vibration acceleration and the centrifugal loading and have a limit, in terms of the centrifugal loading beyond which no damping occurs. The main parameters that influence the performance of the particle dampers are the length/diameter aspect ratio and the particle size. An important finding is that a particle damper with fewer layers (increase in particle size) will still function at a higher centrifugal load, compared with one with more layers.

Nomenclature

A	=	amplitude of oscillations, m
A'	=	effective area, m^2
C_ε	=	strain gauge correction factor
c	=	damping factor, $N \cdot s/m$
c_e	=	equivalent beam damping factor, $N \cdot s/m$
d_c	=	tip container cavity diameter, m
f_n	=	natural frequency, $\omega_n/(2\pi)$, Hz
g_0	=	gravitational acceleration, 9.81 m/s^2
h_c	=	tip container cavity height, m
h_g	=	gap height, $h_c - h_0$, m
h_0	=	average fill height, m
h'_0	=	average effective fill height, m
i, j	=	indices
k	=	spring stiffness, N/m
k_e	=	equivalent beam stiffness, N/m
M_e	=	equivalent tip container mass, kg
m	=	mass, kg
m_c	=	tip container mass, kg
m_e	=	equivalent beam mass, kg
m_p	=	average total particle mass, kg
N	=	number of balls
N_0	=	number of balls in contact with base
n_d	=	number of equivalent layers, $h_0/(2r_i)$
n'_d	=	number of effective layers, $h'_0/(2r_i) = n_d/\lambda$
R	=	rotation radius, 0.4 m
r	=	ball radius, m
r_m	=	mass ratio, m_p/M_e
T	=	period of the damped motion, s
t	=	time, s
y	=	beam tip displacement, m
y_0	=	beam tip displacement at $t = 0$, m
y^*	=	envelope of displacement, m
α	=	particle fraction contributing toward the total mass
Γ	=	peak acceleration amplitude factor, $A\omega^2/g_0$
Γ_R	=	centrifugal acceleration factor, $R(2\pi\Omega)^2/g_0$
δ_A	=	logarithmic decrement
δ_A^*	=	slope of the exponential decay function in log space, s^{-1}
ζ	=	viscous damping factor, $c/(2m\omega_n)$
θ	=	angular parameter, rad
λ	=	container cavity aspect ratio, h_c/d_c
τ_i	=	times at zero crossings where $y(\tau_i) = 0$, s
Ω	=	system rotation velocity, s^{-1}
ω_n	=	natural frequency, $\sqrt{k/m}$, rad/s

Presented as Paper 2009-2688 at the 50th AIAA/ASME/ASCE/AHS/ASC Structures, Structural Dynamics, and Materials Conference, Palm Springs, CA, 4–7 May 2009; received 26 October 2010; revision received 4 April 2011; accepted for publication 12 April 2011.

*Senior Lecturer, Department of Mechanical and Mechatronic Engineering; dnjels@sun.ac.za.

I. Introduction

PARTICLE dampers (PDs) are composed of a container filled with one or more particles (metals, ceramics, etc.). They function by dissipating energy through inelastic impacts and friction between the particles and the walls and between the particles themselves. PDs are simple and inexpensive devices. The range of applications of PDs is vast. Panossian [1] drilled holes in a liquid oxygen inlet tee on the space shuttle main engine, where high-amplitude vibrations caused the formation of cracks. The holes were then filled with metal particles, thereby reducing the vibrations substantially. Simonian [2] attached a PD to the tip of a satellite antenna boom, to reduce vibrations. Ema and Marui [3] improved the damping capability of boring tools and suppression of chatter vibration with PDs. Velichkovich and Velichkovich [4] used a PD to control vibrations during deep oil and gas drilling. Simonian [5] gives an in-depth overview of applications in diverse disciplines such as aerospace, ground transportation, and high-performance sporting equipment industries.

Papalou and Masri [6–8] conducted extensive experimental studies on the influence of mass ratio, particle size, container dimensions, excitation levels, and direction of excitation on the behavior of PDs. They introduced an equivalent single-particle impact damper model, to evaluate the performance of multi-PDs. Saeki [9] investigated the dynamics of an PD in a horizontally vibrating system experimentally. An analytical solution with the discrete element method (DEM) is provided, to estimate the response with reasonable accuracy. Wu et al. [10] developed an analytical model based on multiphase flow theory of granular matter, to evaluate qualitatively the energy dissipation in PDs. Fang and Tang [11] improved it over a wide range of parameters.

Of interest in this study is the performance of PDs under centrifugal loads or acceleration loads in general. In the experimental procedure shown in Figs. 1 and 2, a PD vibrating in the vertical

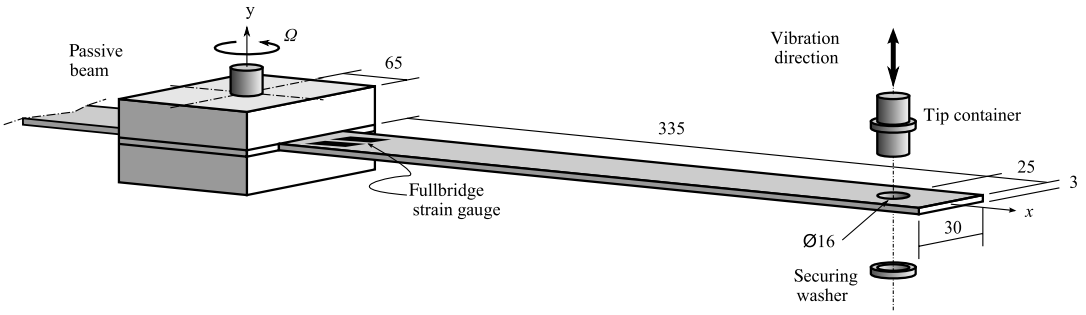

Fig. 1 Schematic layout of test beam assembly (in mm).

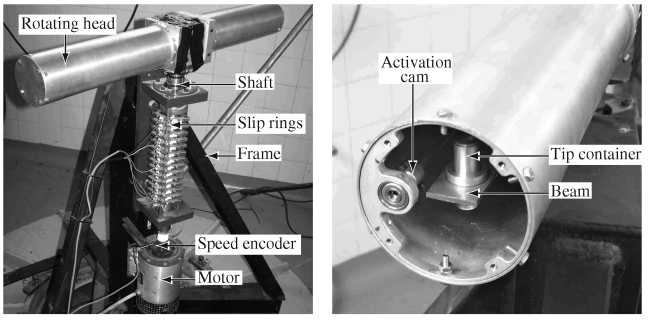

a) Main experimental apparatus **b) Internal parts and activation mechanism**

Fig. 2 Experimental equipment.

direction while under centrifugal loads was investigated. For low centrifugal loads ($\Gamma_R < 1$), the damping characteristics can be compared with those found in the literature for vertical vibration. It is important to realize that, when the centrifugal acceleration exceeds $1g_0$ or $\Gamma_R > 1$, the particles are no longer free to bounce up and down but tend to move along the side wall. If the centrifugal acceleration is further increased, the particles move in a "sloshing" motion along the wall until the centrifugal forces become too high to allow any relative motion between the particles. It is therefore clear that the analysis of PDs in horizontal motion perpendicular to gravity is more appropriate to understand the damper characteristics in this case.

For horizontal vibrations, Liu et al. [12] performed a series of response-level-controlled tests on PDs with different geometries. They found for low-response levels (or effective system acceleration [13]) that the particles act as an added mass, lowering the system resonance frequency. For an increase in response level, the damping increases, and the resonant frequency of the system shifts toward that of the empty PD. It was also found that the cavity aspect ratio (length/diameter) plays an important role in the performance of PDs. Rongong and Tomlinson [14], in a follow-up study, experimentally investigated a large number of parameters affecting PDs. For low-damper aspect ratios, particle fluidization occurs at higher amplitudes. Dampers fluidizing at higher vibration levels have higher energy dissipation. For particle size and material type, they found that it had a significant influence on the energy dissipation, contrary to vertical vibrations. The particles were also coated with an oil film to investigate the effect of friction, and it was found that the oil reduces the amplitude dependence and the damping. This shows that friction is the key driver of PD effectiveness. Witt and Kinra [15] tested various PD configurations under horizontal vibrations. For a single layer of large uniform-sized balls, it was found that the initial clearance between the tightly packed balls and the container wall has no influence on the specific damping capacity for large clearances. They observed significant damping for $0.25 < \Gamma < 1$ and a significant reduction in damping around $\Gamma = 1$. For $\Gamma > 1$, the damping increases again. If the clearance is decreased, a maximum specific damping capacity occurs just below $\Gamma = 1$. For smaller balls with the same total mass, it was found that the clearance has no influence. For multiple layers of balls, the damping increased with an increase in void space between the balls and the container. It was also observed that larger balls damp more effectively, compared with smaller balls with the same total mass.

Very few publications exist in the open literature about PDs under high centrifugal loads, such as in turbine or fan blades. No literature could be found for the lower acceleration regime, such as for banking aircraft or rockets during launch. Panossian [16] simulated centrifugal loading, by applying forces with a pressure piston to the particles inside a damper container for a frequency range up to 5 kHz. A significant decrease in structural vibrations was observed, even when the holes were completely filled and subjected to a pressure of 24 MPa. Wong and Rongong [17] showed that the performance of a PD can be controlled by constraining the movement of the particles with a pressure boundary. They used polyurethane foam to alter the static effective pressure inside the PD. Preliminary tests conducted by Flint [18] showed a PD functioning at high centrifugal loads ($\Gamma_R > 5000$), damping the second bending moment. Flint et al. [19] compiled available data on the excitation acceleration ratios Γ/Γ_R from open publications. It is clear the centrifugal stiffening decreases the amplitude exponentially, despite the increase of resonance frequency with centrifugal loading.

II. Experimental Setup and Calibration

The test bench shown in Fig. 2 was developed to determine the behavior of PDs under centrifugal loads. The main component of the apparatus is a flexible stainless steel beam with an aluminum container at the tip that can be filled with steel balls. The system is symmetric with an identical passive side for balancing purposes. The test beam depicted in Fig. 1 was laser cut from a 3 mm American Iron and Steel Institute grade 304 stainless steel sheet to the dimensions shown.

The tip of the beam is remotely activated with a cam, as shown in Fig. 2. The cam rotates slowly, displacing the tip of the beam. At the point of maximum displacement, the beam slips off the cam and is then free to vibrate. The vibration decay is measured with a full-bridge strain gauge at the root of the beam, as shown in Fig. 1. The strain signal is transferred from the rotating part across slip rings and captured with data acquisition hardware and software. The rotation of the beam and shaft is remotely controlled, and rotation velocity is also measured.

The following design considerations were taken into account during the development of the test bench. The frame and shaft were of a rigid and heavy construction to ensure a natural frequency an order of magnitude higher than that of the test beam. High-tolerance pretensioned bearings were used, and all the rotating parts were dynamically balanced. The beam was enclosed in a tube, to eliminate aerodynamic flow effects during rotation. The symmetric passive beam has a natural frequency close to that of the test beam. It was therefore tied down to prevent transfer of vibrations and excitation of the test side of the apparatus.

A. Measurement Calibration

1. Static Calibration

The full-bridge strain gauge configuration, shown in Fig. 1, measures the difference in strain between the upper and lower surfaces of

the beam, i.e., the strain due to the bending moment on the beam, whereas the strain from axial loads is ignored.

The first calibration test that was performed was to determine the relationship between the beam tip displacement y and the strain gauge output signal under static conditions. It was done by inserting a range of calibrated measurement blocks under the tip container and measuring the output strain signal. The relationship between y and the strain gauge output signal is linear for a displacement range of $-16 \text{ mm} \leq y \leq 16 \text{ mm}$. A linear fit of the test data gives the static calibration constant.

2. *Dynamic Calibration*

When the beam is centrifugally loaded, the centrifugal force on the curved section of the beam increases the bending moment at the root of the beam, resulting in the overestimation of the initial displacement, as depicted by the raw uncorrected values in Fig. 3. This was confirmed with a nonlinear large strain finite element method (FEM) analysis. If the assumption is made that the initial tip displacement of $\Delta y_0 \approx -6.2$ mm from the cam action is constant for all conditions, then the measured data can be corrected after fitting a function through the raw data, as shown in Fig. 3. The correction factor is

$$C_\varepsilon \approx -9.910 \times 10^{-5}\ \Omega^3 + 3.850 \times 10^{-3}\ \Omega^2 + 6.372 \times 10^{-3}\ \Omega + 1 \tag{1}$$

It is important to note that Eq. (1) is only valid for the reference tip container with total mass of 28.34 g, with which all the damping experiments were performed. The same procedure was followed for the other container masses used in Sec. II.B, but the equations are not shown here.

For the displacement measurement under dynamic conditions, while the beam is vibrating, it is assumed that the static loaded beam shape is close to the first vibration mode shape at the maximum deflection point. It is therefore assumed that the resulting error in calculation of the maximum deflection is small. It is an open question whether the static calibration remains linear with centrifugal loading.

The issue of what exactly is measured with the strain gauges under dynamic conditions may be resolved by attaching accelerometers to the beam tip to correlate the measurements, or by performing a three-dimensional, large strain dynamic FEM simulation to verify the results. Such a study is outside the scope of this research, and the approximations discussed here will be used instead, due to the sole interest in the frequency and the peak displacement values.

B. System Characterization Tests

For the rotating beam in the experimental setup, the assumption is made that it can be approximated as a single-degree-of-freedom (SDOF) system but with increased stiffness and total added mass because of centrifugal effects. It is also assumed that the force–displacement relationship stays linear. For the system characterization, an equivalent SDOF mass–spring–damper system needs to be found that will behave the same as the beam–mass system under dynamic situations.

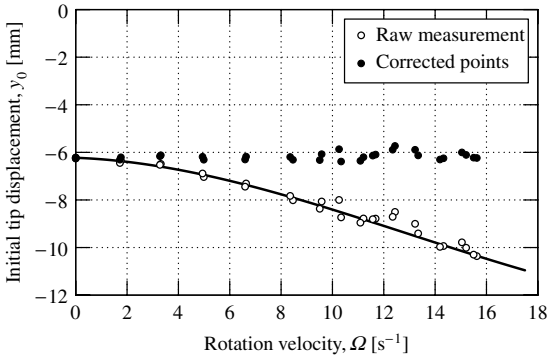

Fig. 3 Correction of tip displacement in relation to rotation for a reference tip container with mass of 28.34×10^{-3} kg.

1. *Test Procedure*

A series of tests was conducted over a range of rotation velocities from 0 to 17 s^{-1} (0 to 1000 min^{-1}), with three different tip masses:

$$\begin{aligned} m_0 &= 0.00 \times 10^{-3} \text{ kg} - m_{\text{hole}} = -4.77 \times 10^{-3} \text{ kg} \\ m_1 &= 13.65 \times 10^{-3} \text{ kg} - m_{\text{hole}} = 8.88 \times 10^{-3} \text{ kg} \\ m_2 &= 28.34 \times 10^{-3} \text{ kg} - m_{\text{hole}} = 23.57 \times 10^{-3} \text{ kg} \end{aligned} \tag{2}$$

For every test, the test bench was spun to the desired velocity, and after the speed and strain gauge readout stabilized the beam was activated. The strain gauge and velocity output were then recorded at a resolution of 2.4 kHz for 20 s or more. At least two readings were taken at each rotational speed.

2. *Data Analysis*

Although great care was taken to balance the equipment and pretension the bearings, it was found during physical vibration measurements that the rotation of the equipment did induce a forced vibration on the beam. Furthermore, the tip of the beam is released from a slow rotating off-centered cam, resulting in the excitation of higher bending and torsion vibration modes. These higher-order modes have an order of magnitude higher frequency and small amplitudes compared with the first bending mode and are therefore ignored in this analysis.

To analyze the test data, the SDOF mass–spring–damper system with base excitation [20] was used. A Levenberg–Marquardt data fit algorithm [21] was used to extract the natural frequency f_n of the first vibration mode and the viscous damping coefficient ζ from the test data. The results are given in Figs. 4a and 4b.

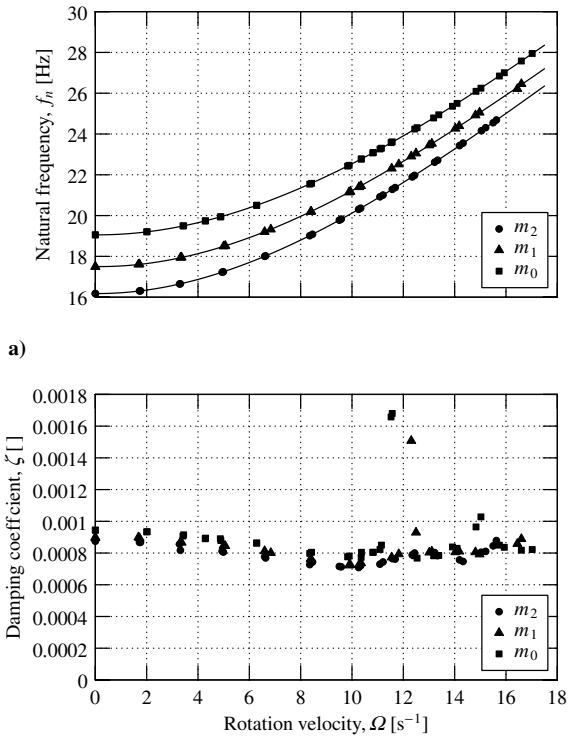

Fig. 4 Calibration tests: a) natural frequency f_n of the first vibration mode of the beam and b) damping coefficient ζ of the beam in relation to the rotation velocity for different tip masses.

Table 1 Frequency polynomial coefficients

i	a_{i0}	a_{i1}	a_{i2}	a_{i3}
0	19.05684	-1.03891×10^{-2}	4.242124×10^{-2}	-6.549958×10^{-4}
1	17.50218	-1.91806×10^{-2}	4.763546×10^{-2}	-8.501543×10^{-4}
2	16.17699	-9.40016×10^{-3}	4.917415×10^{-2}	-8.805505×10^{-4}

3. Equivalent Mass Determination

Third-order polynomials were fitted to the three data sets in Fig. 4a and are shown as the continuous lines in the figure. Let

$$f_{n_i}(\Omega) = \sum_{j=0}^{3} a_{ij}\Omega^j \qquad i = 0, 1, 2 \tag{3}$$

with the polynomial coefficients a_{ij} given in Table 1.

The equivalent beam mass m_e is the mass contribution of the beam in an equivalent SDOF mass–spring–damper system. The equivalent stiffness k_e of the beam in terms of m_e is

$$k_e = \omega_{n_i}^2(m_e + m_i) = 4\pi^2 f_{n_i}^2(m_e + m_i), \qquad i = 0, 1, 2 \tag{4}$$

Note that the assumption is made that the centrifugal load on the tip mass does not contribute toward the overall stiffness of the total system or that k_e and m_e are independent of the added tip mass for the mass range used. Equation (4) can be solved in a least-squares fashion for m_e:

$$m_e = \frac{(\Sigma f_{n_i}^2 m_i)(\Sigma f_{n_i}^2) - 3\Sigma f_{n_i}^4 m_i}{3\Sigma f_{n_i}^4 - (\Sigma f_{n_i}^2)^2} \tag{5}$$

The numerical values of $m_e = m_e(\Omega)$ in Eq. (5) were calculated at discrete values of $f_{n_i}(\Omega)$, and the result is depicted in Fig. 5. For numerical purposes, Eq. (5) can be approximated with a polynomial:

$$m_e(\Omega) \approx -7.58716 \times 10^{-7}\ \Omega^4 + 1.86302 \times 10^{-5}\ \Omega^3 + 2.22830 \times 10^{-4}\ \Omega^2 + 4.85802 \times 10^{-4}\ \Omega + 0.077526 \tag{6}$$

4. Equivalent Stiffness and Damping Determination

From the test data, the stiffness k_e and damping factor c_e can be calculated. This is calculated at every measured data point j at rotation velocity Ω_j for the different tip masses m_i. The natural frequency $f_{n_{ij}}$, damping coefficient ζ_{ij} in Figs. 4a and 4b then give

$$k_{e_{ij}} = 4\pi^2 f_{n_{ij}}^2[m_e(\Omega_j) + m_i] \tag{7}$$

$$c_{e_{ij}} = 4\pi\zeta_{ij} f_{n_{ij}}[m_e(\Omega_j) + m_i] \tag{8}$$

for $i = 0, 1, 2$ and $j = 0, \cdots, N$.

The results are depicted in Figs. 6a and 6b and can be approximated with the following polynomials:

$$k_e(\Omega) \approx 0.48077\ \Omega^3 + 6.2839\ \Omega^2 - 7.2071\ \Omega + 1046.1 \tag{9}$$

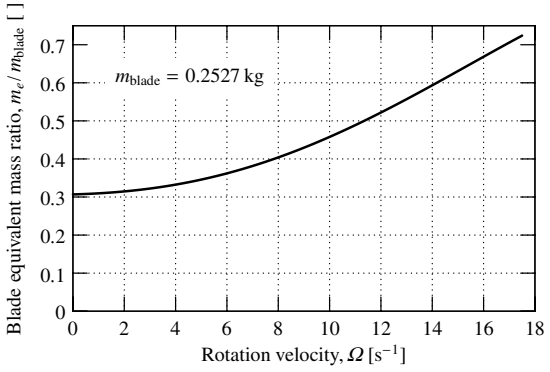

Fig. 5 Equivalent beam mass ratio in relation to rotation velocity.

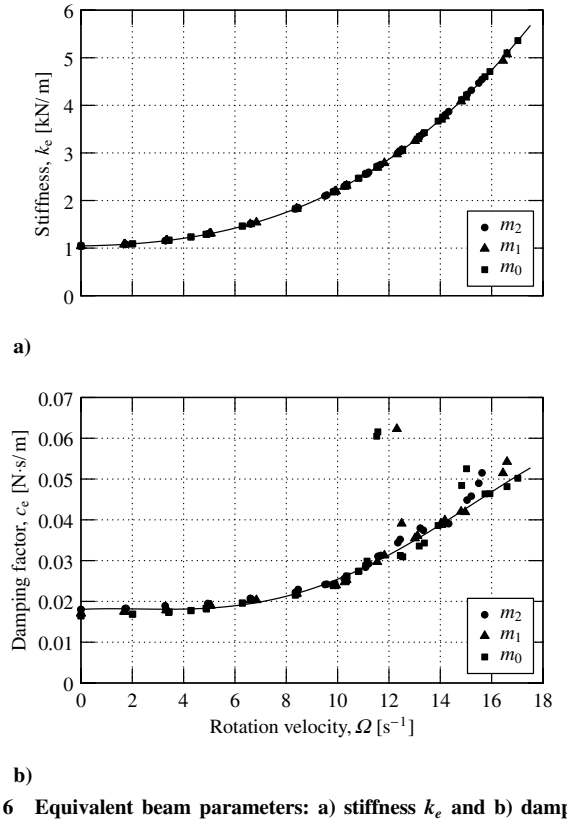

Fig. 6 Equivalent beam parameters: a) stiffness k_e and b) damping factor c_e in relation to rotation velocity for different tip masses.

$$c_e(\Omega) \approx -9.1735 \times 10^{-7}\ \Omega^4 + 3.2263 \times 10^{-5}\ \Omega^3 - 1.8864 \times 10^{-4}\ \Omega^2 + 3.1662 \times 10^{-4}\ \Omega + 0.0180 \tag{10}$$

The assumption in Eq. (4) that the centrifugal load on the tip mass does not contribute toward the overall stiffness is justified in Fig. 6a, in which the k_e values for all three tip mass load cases fall on the same curve.

III. Experimental Analysis of Particle Dampers

The main purpose of the experimental analysis of the PDs was to determine the effect of centrifugal loading on their performance. The damping performance constitutes two parameters, namely the damping coefficient and the minimum excitation acceleration at which the damper is still active.

A. System Parameters

The experiments were designed to eliminate as many system variations as possible. This was achieved by keeping the total tip mass as constant as possible for all the tests. The following configurations were used:

1) Four tip containers with identical masses but different cavity heights were manufactured (see Fig. 7 and Table 2).

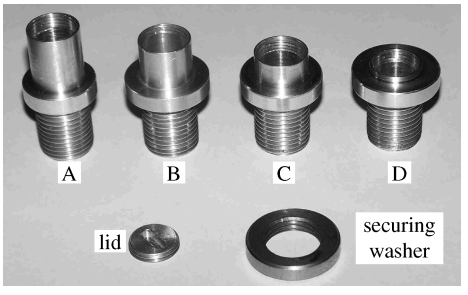

Fig. 7 Set of four different containers used during damper tests.

Table 2 Container parameters

Container	h_c, mm	d_c, mm	$\lambda = h_c/d_c$	m_c, kg
A	37.0	12.5	2.96	21.52×10^{-3}
B	31.0	12.5	2.84	21.57×10^{-3}
C	25.3	12.5	2.02	21.54×10^{-3}
D	21.8	12.5	1.74	21.51×10^{-3}
——	——	——	——	Average 21.54×10^{-3}

Table 3 Ball parameters

Ball size, mm	No. of balls	m_p, kg
Ø2	207	6.75×10^{-3}
Ø3	62	6.73×10^{-3}
Ø4	26	6.74×10^{-3}

2) Three sizes of steel ball bearings, Ø2 mm, Ø3 mm, and Ø4 mm, were used (see Table 3).

The number of balls selected were to give the same total tip mass (tip container mass plus ball mass) for all the tests. The total tip mass also corresponds with the tip mass used for calibration in Sec. II.A.

The equivalent SDOF properties of the beam were determined in Sec. II.B. The equivalent beam mass m_e in terms of the rotation velocity Ω (in s^{-1}) is given by Eq. (6). The equivalent empty container mass M_e is the sum of the equivalent beam mass m_e and the average empty container mass m_c minus the mass removed from the hole in the beam. From Eq. (6), Table 2, and Fig. 1,

$$m_c = 0.02154 \text{ kg} \tag{11}$$

$$M_e = m_e + m_c - 0.00477 \text{ kg} = m_e + 0.01677 \text{ kg} \tag{12}$$

The average total particle mass from Table 3 is $m_p = 6.74 \times 10^{-3}$ kg. The ratio r_m between the total particle mass and the equivalent SDOF container vibrating mass is defined as

$$r_m = m_p/M_e \tag{13}$$

The centrifugal load on the particles can be given in dimensionless form by the centrifugal acceleration factor:

$$\Gamma_R = R(2\pi\Omega)^2/g_0 \tag{14}$$

with $R = 0.4$ m the system rotation radius and Ω the system rotation velocity (in s^{-1}).

B. Test Procedure

A series of 12 tests was conducted, with four containers and three different ball sizes for each container. For each container/ball test, a range of test was done, with rotation velocities Ω between 0 and 18.3 s^{-1} (1100 min^{-1}). It was found that for $\Omega > 5.8$ s^{-1} (350 min^{-1}) the PD has no influence. Two tests were conducted for every rotation velocity.

C. General Observations

The tip displacement data were calculated from the strain gauge output, using the same procedure as outlined in Sec. II.A. In Fig. 8a, a typical output of the raw displacement data is shown.

Insight into the test data can be gained if the vibration peaks are plotted on a log-scale graph, as depicted in Fig. 8b. It is clear that there are zones of exponential decay or viscous damping present. Zone 1 is the region of high damping. In zone 2, the damping is an order lower, and in zone 3 no damping is present except the inherent damping of the beam itself. Amplitudes A_1, A_2, and A_3 give the displacement range of each zone. The initial displacement is $A_0 = A_1$, and A_3 is the minimum amplitude above which the PD still functions.

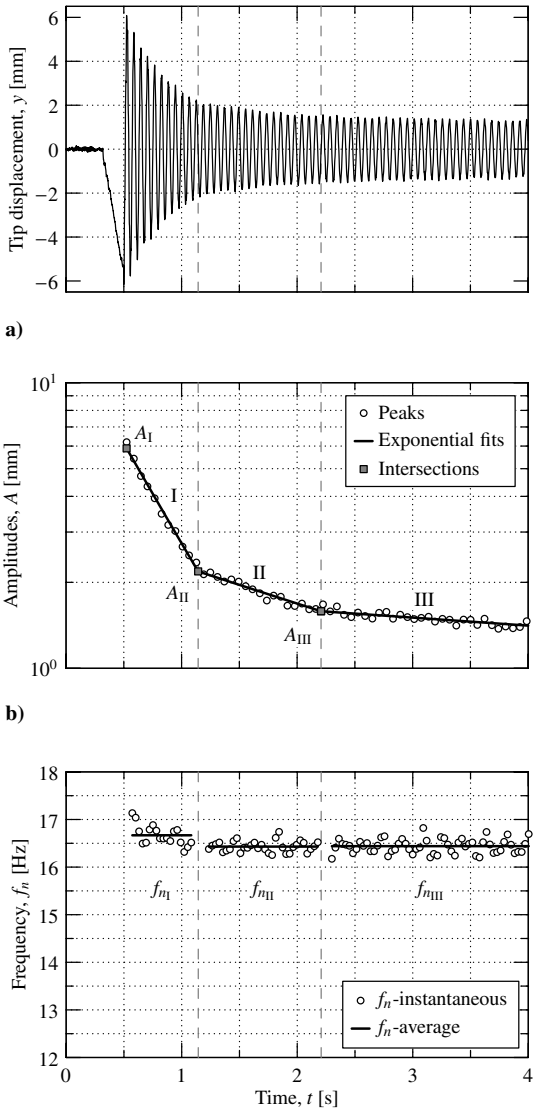

Fig. 8 Example data for container A with Ø4 mm balls and rotation velocity of $\Omega = 2.3$ s^{-1}: a) raw tip displacement data, b) peak amplitudes, and c) instantaneous frequencies.

One or both of zones 1 and 2 were present in all but a few of the tests. For no rotation ($\Omega = 0$ s^{-1}), a few instances were observed in which the decay was not exponential but linear, suggesting friction damping. The results of those tests are not included in the overall analysis.

D. Data Analysis

Based on the fact that the decay in motion is exponential, the system was approximated as a SDOF mass–spring–damper system. The equation of motion for the free decay of an underdamped system, $0 < \zeta < 1$, is given by [20]:

$$y(t) = Ae^{-\zeta\omega_n t}\cos(\sqrt{1-\zeta^2}\omega_n t - \phi) \tag{15}$$

The period T of the damped motion is

$$T = \frac{2\pi}{\omega_n\sqrt{1-\zeta^2}} \tag{16}$$

1. Instantaneous Frequency

Consider the ith peak of the vibration displacement at time t_i at the local maximum, $\cos(\sqrt{1-\zeta^2}\omega_n t_i - \phi) = 1$; then,

$$A_i = y(t_i) = Ae^{-\zeta\omega_n t_i} \tag{17}$$

The ratio between two successive peaks is

$$\frac{A_i}{A_{i+1}} = \frac{y(t_i)}{y(t_i+T)} = e^{2\pi\zeta/\sqrt{1-\zeta^2}} \tag{18}$$

or

$$\ell n\,\frac{A_i}{A_{i+1}} = \ell n\,A_i - \ell n\,A_{i+1} = \frac{2\pi\zeta}{\sqrt{1-\zeta^2}} = \delta_A \tag{19}$$

with δ_A the logarithmic decrement of the peaks. The damping coefficient can be obtained from Eq. (19), in terms of the logarithmic decrement δ_A, with

$$\zeta = \frac{\delta_A}{\sqrt{4\pi^2+\delta_A^2}} \tag{20}$$

Consider Fig. 8b. The time varying envelope of motion of Eq. (15) modulating the cosine function is given by

$$y^*(t) = Ae^{-\zeta\omega_n t} \tag{21}$$

Equation (21) can be written in logarithmic format:

$$\ell n\,y^*(t) = \ell n\,A - \zeta\omega_n t = \ell n\,A - \delta_A^* t \tag{22}$$

with δ_A^* the linear slope of the exponential decay function in log space. The numerical value of δ_A^* can be obtained with a linear regression curve fit on the peak data against time, in Fig. 8b, for zones 1, 2, or 3.

For t_i, the time at the ith peak is the decrement in peak values:

$$\ell n\,y^*(t_i) - \ell n\,y^*(t_i+T) = \ell n\,A_i - \ell n\,A_{i+1} = \delta_A^* T \tag{23}$$

It is clear from Eqs. (19) and (23) that $\delta_A = \delta_A^* T = \omega_n \zeta T$. If this result is inserted into Eq. (20), the frequency is obtained:

$$\omega_n = \sqrt{\frac{4\pi^2}{T^2} - \delta_A^{*2}} \tag{24}$$

From Fig. 8a, the $N+1$ points can be found where the signal crosses zero. Through interpolation, the times $t = \tau_j$ where $y(\tau_j) = 0$ for $j = 0, 1, \ldots, N$ can be found. The instantaneous period of the signal at time τ_ℓ is then defined as

$$T_\ell = \tau_{\ell+1} - \tau_{\ell-1}, \qquad \ell = 1, 2, \ldots, N-1 \tag{25}$$

The instantaneous vibration frequency at time τ_ℓ is then given by

$$\omega_n(\tau_\ell) = 2\pi f_n(\tau_\ell) = \sqrt{\frac{4\pi^2}{T_\ell^2} - \delta_A^{*2}} \tag{26}$$

The result of the application of Eq. (26) on the example is shown in Fig. 8c. It can be seen that the average frequency is about 1.4% higher in zone 1, compared with zones 2 and 3.

2. *Viscous Damping Coefficient*

The average frequency in zones 1, 2, or 3 is defined as

$$\bar{\omega}_n = \frac{1}{N-1}\sum_{k=1}^{N-1}\omega_n(\tau_k) \tag{27}$$

The result is shown by the solid lines in Fig. 8c, for an example. The viscous damping coefficient ζ for each zone can then be calculated from

$$\zeta = \frac{\delta_A^*}{\bar{\omega}_n} \tag{28}$$

with δ_A^* the linear slope of the exponential decay function in log space.

3. *Effective Mass*

The natural frequency of a SDOF mass–spring system is $\omega_n^2 = k/m$, with k the stiffness of the spring and m the mass of the system:

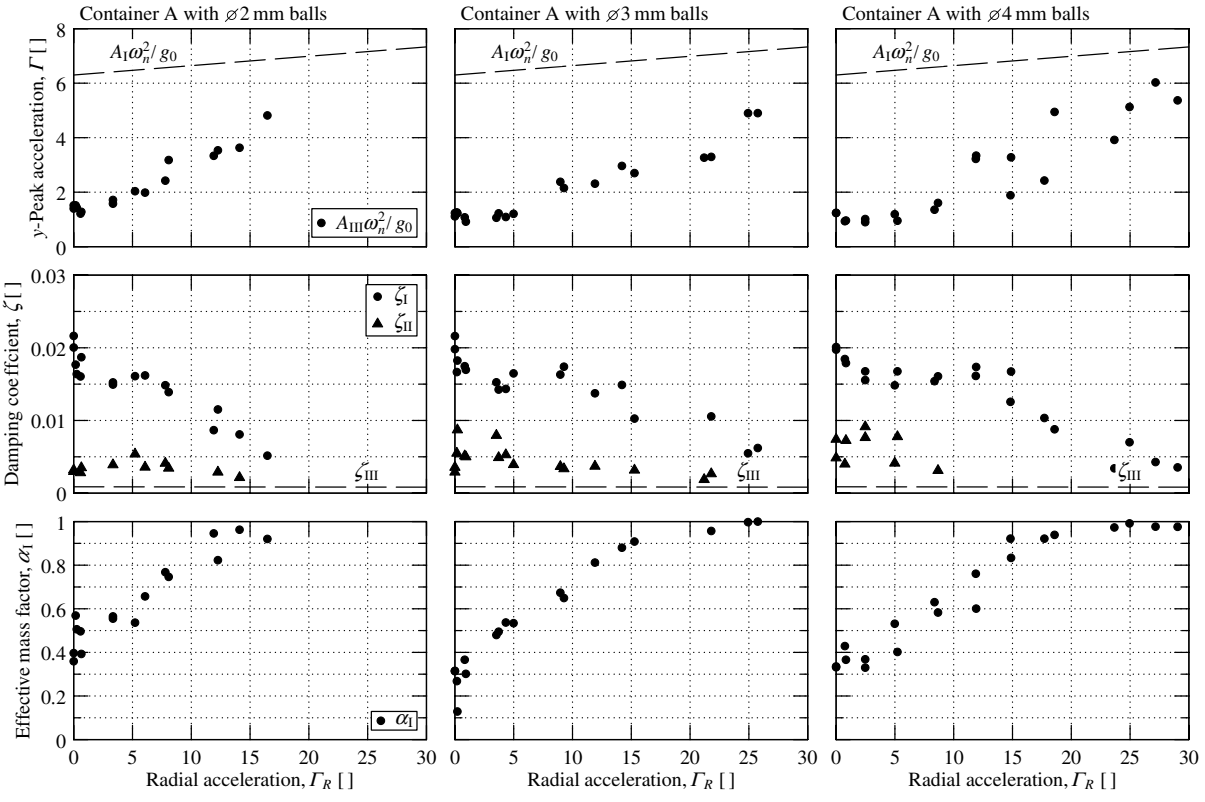

Fig. 9 Test results for container A.

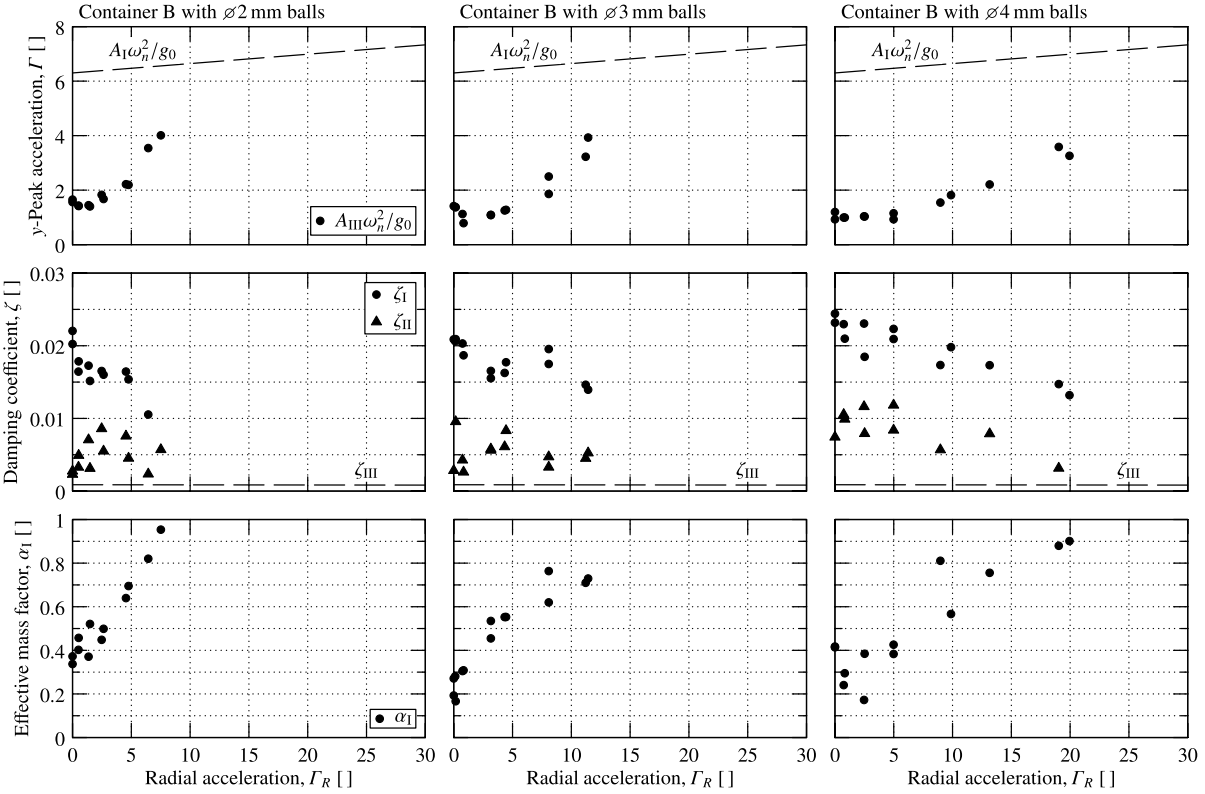

Fig. 10 Test results for container B.

$$\omega_n^2 = \frac{k}{M_e + \alpha m_p} \tag{29}$$

with M_e the effective mass of the beam and container, m_p the mass of the particles, and α the fraction of the particles contributing toward the total mass of the system in zone 1, 2, or 3.

If it is assumed that the stiffness of the spring and the effective mass are constant, then for the frequency to change the contribution of the particle toward the mass of the vibrating system must be variable. In zone 3, there is no particle damping, and the assumption is made that the full mass of particles is part of the total mass of the vibrating system:

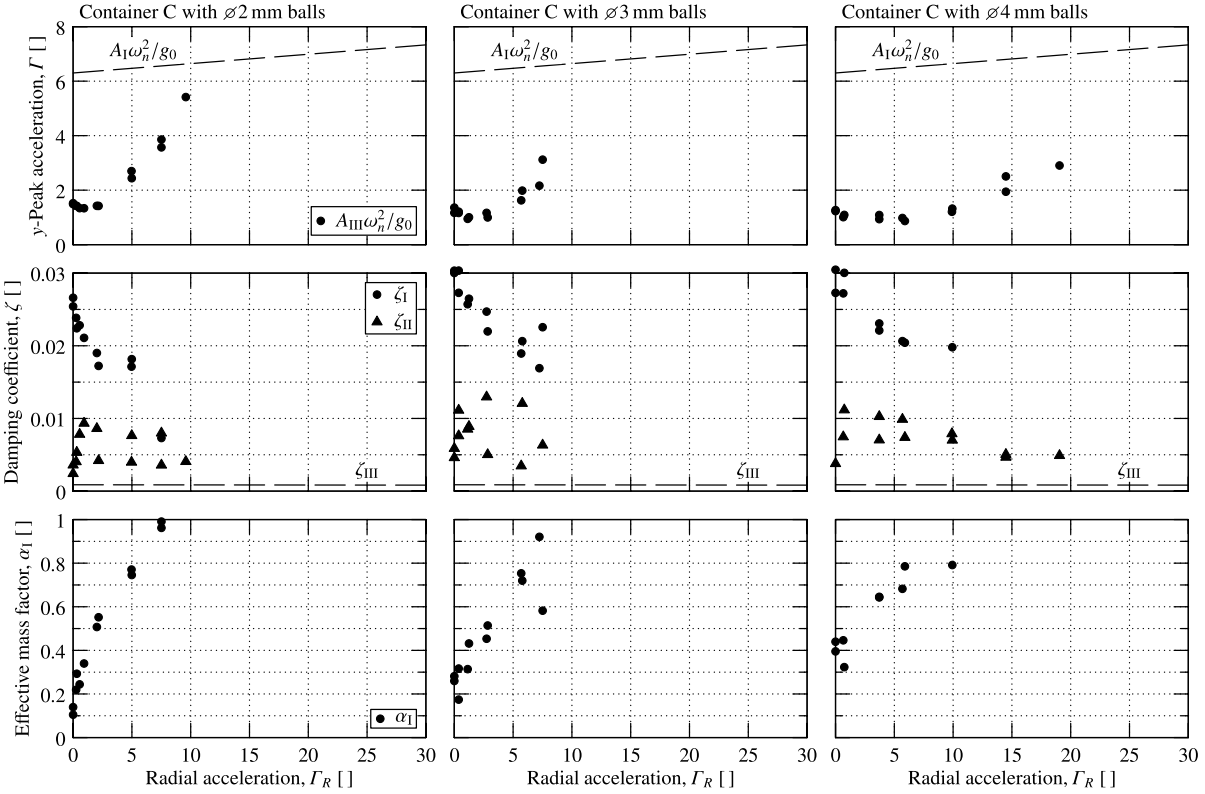

Fig. 11 Test results for container C.

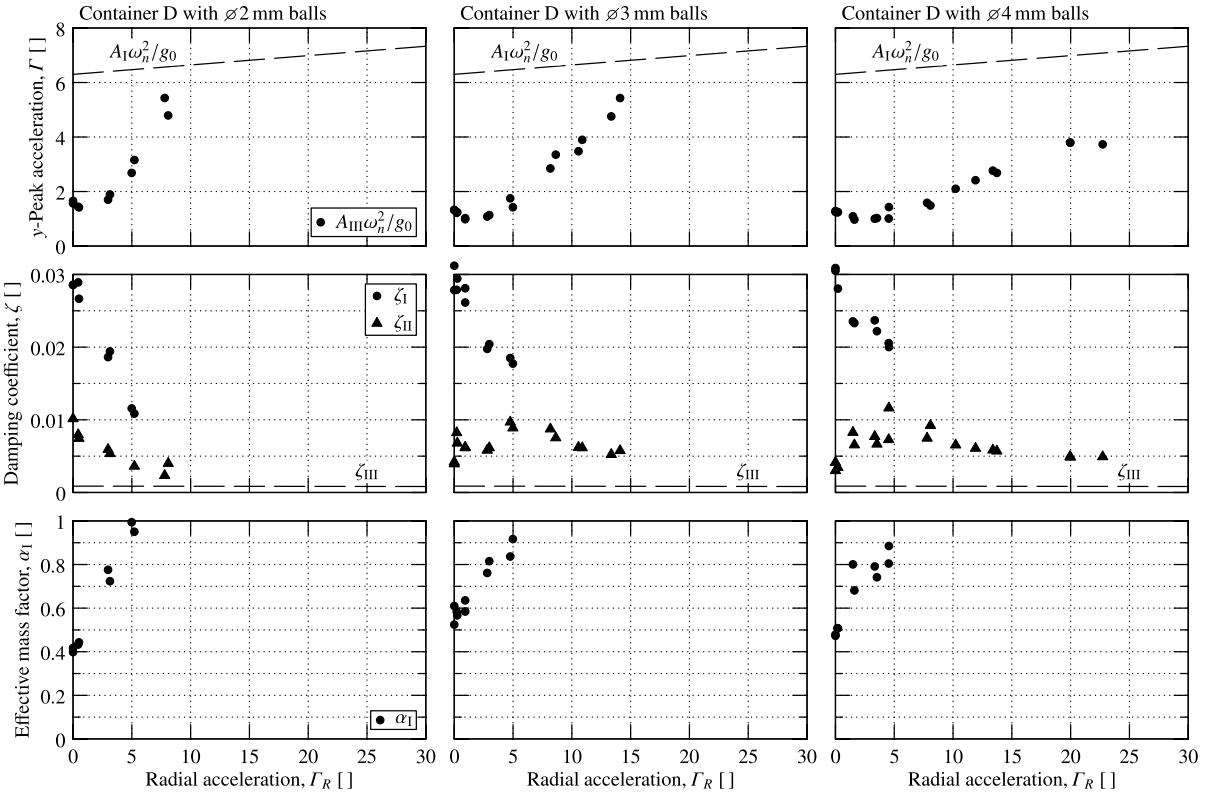

Fig. 12 Test results for container D.

$$\left(\frac{\bar{\omega}_{n_3}}{\bar{\omega}_{n_1}}\right)^2 = \frac{M_e + \alpha_1 m_p}{M_e + m_p} = \frac{1 + \alpha_1 r_m}{1 + r_m} \tag{30}$$

or

$$\alpha_1 = \frac{1}{r_m}\left[\left(\frac{\bar{\omega}_{n_1}}{\bar{\omega}_{n_3}}\right)^2 (1 + r_m) - 1\right] \tag{31}$$

The range of the effective mass factor α_1 is $0 \le \alpha_1 \le 1$. When $\alpha_1 \to 0$, it means that the system is highly excited and that the particles contribute very little toward the system mass. If $\alpha_1 = 1$, then the particles move as a solid unit together with the container.

E. Test Results

The test data have been analyzed as discussed in the preceding sections. The full set of results is given in Figs. 9–12. For every test series, the following results are shown: 1) the change in the operational envelope of the PD, in terms of the peak vibration acceleration amplitude in relation to the centrifugal acceleration factor Γ_R; the peak acceleration amplitude factor in dimensionless form is defined as

$$\Gamma = \frac{A\omega_n^2}{g_0} \tag{32}$$

with ω_n the vibration frequency, A the vibration amplitude, and $g_0 = 9.81$ m/s^2 the gravitational acceleration; 2) the change of the damping coefficient ζ for zones 1 and 2, in relation to the centrifugal acceleration factor Γ_R; and 3) the change in the effective mass factor α_1, in relation to the centrifugal acceleration factor Γ_R; this is an indication of the excitation state of the particles or the relative motion between the particles and the container.

Further data analysis and an in-depth look at the data are shown in the next section.

IV. Detailed Data Analysis

A. System Parameters

1. *Container Aspect Ratio*

The container cavity aspect ratio (length/diameter)

$$\lambda = \frac{h_c}{d_c} \tag{33}$$

is identified in the literature as one of the significant parameters influencing the performance of PDs vibrating perpendicular to gravity [12,22]. The cavity aspect ratios λ are listed in Table 2.

2. *Fill Height and Equivalent Layers*

The true fill height of the balls inside the PD container cannot be measured directly, because the top layer is generally incomplete. In this section, the fill height is calculated indirectly, with DEM simulations of the balls inside the container.

Fifteen different, randomly generated fills for each ball size were generated. The balls were left to settle under gravity, and afterwards the coordinates of the centers of each ball were saved to a file for data processing. The procedure followed to obtain the fill height is illustrated in Fig. 13. The y-coordinates (vertical coordinates) for

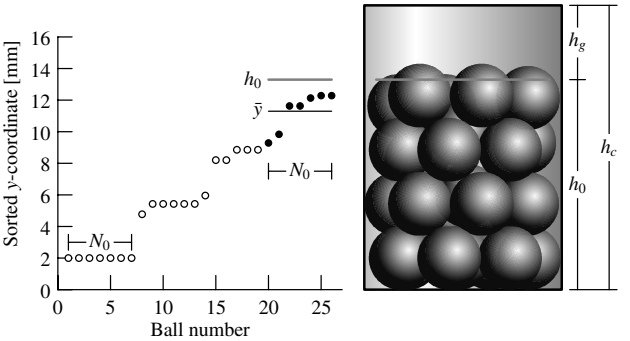

Fig. 13 Example of fill height calculations for Ø4 mm balls.

Table 4 Ball fill parameters

Ball size	r_i, mm	N	h_0, mm	n_d	h_g, mm A	B	C	D
Ø2 mm	1.0	207	12.8 ± 0.1	6.3	24.2	18.2	12.5	9.0
Ø3 mm	1.5	64	13.6 ± 0.3	4.5	23.4	17.4	11.7	8.2
Ø4 mm	2.0	26	13.4 ± 0.4	3.3	23.6	17.6	11.9	8.4

each set were sorted from small to large. The number of balls in contact with the base of the container was counted and denoted by N_0. The assumption was made that this is the effective number of balls in a layer. If N is the total number of balls, then the average height of the N_0 highest balls is the average effective fill height:

$$h_0 = r_i + \bar{y} \quad \text{with} \quad \bar{y} = \frac{1}{N_0} \sum_{i=N-N_0}^{N} y_i \tag{34}$$

The number of equivalent layers is defined as

$$n_d = \frac{h_0}{2r_i} \tag{35}$$

The calculated average effective fill heights and number of equivalent layers are listed in Table 4. The tolerance of h_0 is one standard deviation.

Under centrifugal loads, the particles move against the side of the container. The fill volume of the particles under centrifugal load can be calculated as

$$\frac{\pi d_c^2 h_0}{4} = A' h_c = \frac{d_c^2 h_c}{8}(\theta - \sin\theta) \tag{36}$$

with A' the area of the sector, as shown in Fig. 14. Rewrite Eq. (36) as

$$\frac{h_0}{h_c} = \frac{1}{2\pi}(\theta - \sin\theta) \tag{37}$$

From the geometry in Fig. 14, the height h_0' of the sector area A' is

$$\frac{h_0'}{d_c} = \frac{1}{2}\left(1 - \cos\frac{1}{2}\theta\right) \tag{38}$$

From the parametric plot of h_0/h_c and h_0'/d_c as functions of θ, in Fig. 14, it is clear that the relationship between the parameters can be approximated as

$$\frac{h_0'}{d_c} \approx \frac{h_0}{h_c} \quad \text{or} \quad h_0' \approx h_0 \frac{d_c}{h_c} = \frac{h_0}{\lambda} \tag{39}$$

with λ the container cavity aspect ratio (length/diameter), given in Eq. (33).

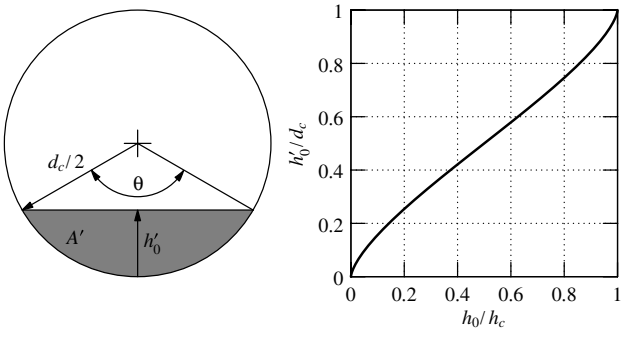

Fig. 14 Fill height calculations for balls against side wall.

The number of effective layers under centrifugal load can then be defined as

$$n_d' = \frac{h_0'}{2r_i} \approx \frac{n_d}{\lambda} \tag{40}$$

3. Gap Height

The clearance or gap height or free space between the balls and the top lid of the container is

$$h_g = h_c - h_0 \tag{41}$$

Table 3 lists the container heights h_c, and Table 4 the gap heights.

Note that the fill height h_0 is more or less constant in Table 4. It is therefore not possible to distinguish between the effects of the gap height and the cavity aspect ratio, because they are directly related for this experimental setup.

B. Parameter Correlations

1. Definitions

In the design of the experimental apparatus, the decision was taken to use a constant tip or PD mass. The parameters that vary for each PD configuration are listed in Tables 2 and 4. The fill height h_0 can be taken as constant. The number of equivalent layers n_d varies with ball size but is independent of the container type. The gap height h_g, on the other hand, varies with container type but is independent of the ball size for all practical purposes, and the cavity aspect ratio λ varies only with container type. Only the aspect ratio and not the fill height will be considered, because they are directly related.

The next step is to investigate the influence of n_d and λ on the performance of PDs under centrifugal loads, by scaling the parameters in the performance graphs (Figs. 9–12). To compare the different configurations, define the following scaling parameters:

$$n_{d_i}^* = n_{d_i}/n_{d_{ref}} \quad \text{with} \quad i = \text{Ø2 mm, Ø3 mm, Ø4 mm} \tag{42}$$

and

$$\lambda_j^* = \lambda_j/\lambda_{\text{ref}} \quad \text{with} \quad j = \text{A, B, C, D} \tag{43}$$

Container A, with Ø4 mm balls, was taken as reference and $n_{d_{\text{ref}}} = 6.3$ and $\lambda_{\text{ref}} = 2.96$ as the reference values.

2. Parameter Scaling Results

The objective with the parameter comparisons was to obtain general trends and not accurate curve fits for all the data. Of interest are the regions with a significant centrifugal acceleration ($\Gamma_R > 1$). The procedure followed was first to compare a single container filled with different ball sizes. In this way the influence of the number of equivalent layers n_d could be established. The second step was to compare a single ball size in different containers for an indication of the influence of the cavity aspect ratio λ. Figure 15 shows the final results of the effects of parameter scalings.

The important observation from this figure is that all the PD performance parameters scale as a function of the centrifugal acceleration $\Gamma_R n_d^*/\lambda^* = \Gamma_R n_d'^*$. This implies that a PD will function at higher centrifugal loads if the number of effective layers n_d' is decreased.

For the performance parameters individually, it was found that the damping envelope, or the minimum peak vibration acceleration at which the PD still functions, scale as $\Gamma/\sqrt{n_d^*}$. This indicates that a decrease number of layers (larger balls) will result in a lower peak vibration acceleration Γ at which damping still occurs. The damping factor in zone 1 scales as $\zeta_I \sqrt{\lambda^*}$. This indicates that an increase in the cavity aspect ratio decreases the damping factor. The relationship between the cavity aspect ratio and the damping factor corresponds with the general trends found in the literature. The effective mass factor scales as $\alpha_1 \sqrt{\lambda^*}$. An increase in λ will reduce α_1, which can be interpreted as a more energetic motion of the balls.

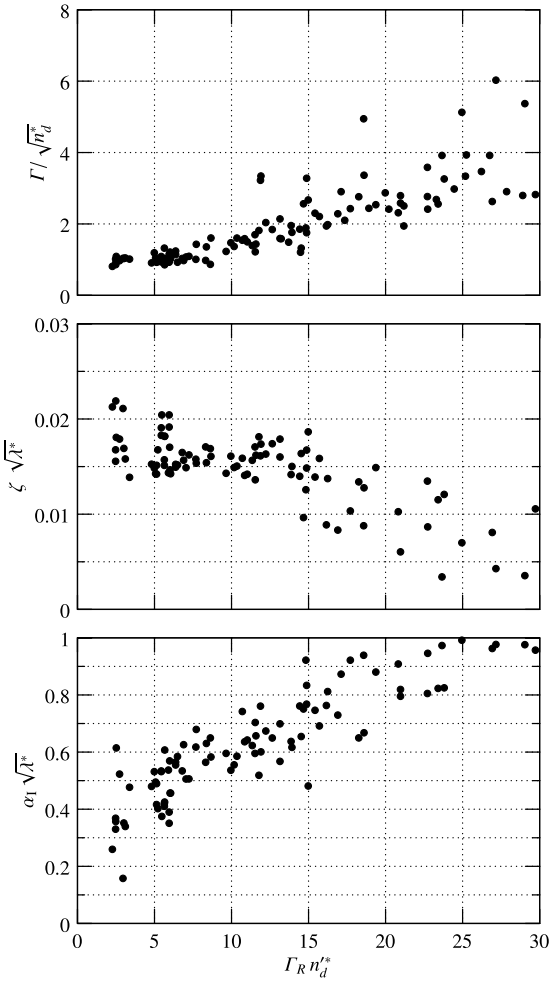

Fig. 15 Parameter correlations for all the test data ($\Gamma_R > 1$).

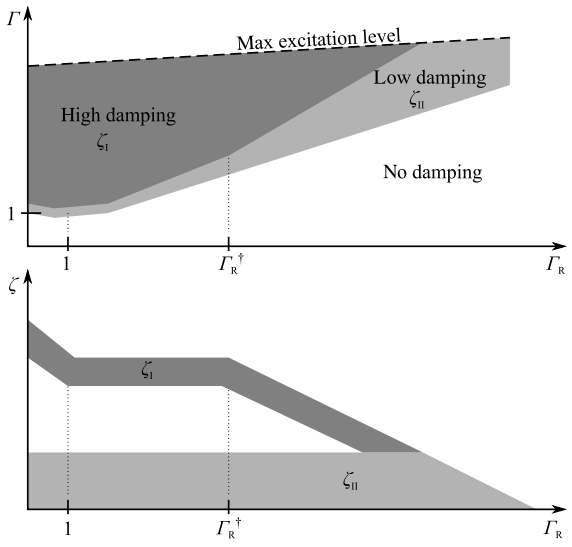

Fig. 16 PD performance factors.

V. Conclusions

The main purpose of this study was to determine the effect of centrifugal loading on the damping performance of PDs. The damping performance constitutes two parameters: the damping coefficient ζ and the minimum excitation acceleration at which the damper is still active (damping envelope). Figure 16 gives a summation of the general trends observed in the test data, from Figs. 9–12.

From the data analysis in Sec. III, it can be concluded that there are two zones of damping, one with a high- and one with a low-damping factor (ζ_1 and ζ_2). These damping zones depend on the ratio between the peak vibration acceleration and the centrifugal loading. Each zone has a limit, in terms of the centrifugal loading beyond which the PD cannot function if the vibration amplitude is fixed. In the high-damping zone, it was found that the excitation state of the particles was high enough to move relative to the container, thereby causing the system vibration frequency to change. In the low-damping zone, there is only limited motion between the particles.

It is also noticeable that the damping factor in the high-damping zone is approximately constant for centrifugal loads of more than $1g_0$ up to the load point, where the high-excitation state of the particles disappears ($\Gamma_R^\dagger$ in Fig. 16). This constant region is highly dependent on the PD container depth and can be increased with a container with a larger depth (or aspect ratio).

In the extended analysis of Sec. IV, it was found that the main parameters that influence the performance of the PDs are the PD cavity length/diameter aspect ratio and the particle size:

1) A decrease in the number of layers (larger balls) results in a lower vibration acceleration Γ at which damping still occurs.

2) An increase in the cavity aspect ratio λ decreases the damping factor.

3) An important finding is that a PD with less layers (increase in particle size) will still function at a higher centrifugal load, compared with one with a larger number of layers.

References

[1] Panossian, H. V., "Structural Damping Enhancement via Non-obstructive Particle Damping Technique," *Journal of Vibration and Acoustics*, Vol. 114, No. 1, 1992, pp. 101–105. doi:10.1115/1.2930221

[2] Simonian, S. S., "Particle Beam Dampers," *Proceedings of SPIE Conference on Smart Structures and Materials: Passive Damping*, edited by C. D. Johnson, Vol. 2445, San Diego, CA, March 1995, pp. 149–160.

[3] Ema, S., and Marui, E., "Suppression of Chatter Vibration of Boring Tools Using Impact Dampers," *International Journal of Machine Tools and Manufacture*, Vol. 40, No. 8, 2000, pp. 1141–1156. doi:10.1016/S0890-6955(99)00119-4

[4] Velichkovich, A. S., and Velichkovich, S. V., "Vibration-Impact Damper for Controlling the Dynamic Drillstring Conditions," *Chemical and Petroleum Engineering*, Vol. 37, Nos. 3–4, 2001, pp. 213–215. doi:10.1023/A:1017650519261

[5] Simonian, S. S., "Particle Damping Applications," 45th AIAA/ASME/ASCE/AHS/ASC Structures, Structural Dynamics and Materials Conference, AIAA Paper 2004-1906, Palm Springs, CA, 19–22 April 2004.

[6] Papalou, A., and Masri, S. F., "Performance of Particle Dampers Under Random Excitation," *Journal of Vibration and Acoustics*, Vol. 118, No. 4, 1996, pp. 614–621. doi:10.1115/1.2888343

[7] Papalou, A., and Masri, S. F., "Response of Impact Dampers with Granular Materials Under Random Excitation," *Earthquake Engineering and Structural Dynamics*, Vol. 25, No. 3, 1996, pp. 253–267. doi:10.1002/(SICI)1096-9845(199603)25:3<253::AID-EQE553>3.0.CO;2-4

[8] Papalou, A., and Masri, S. F., "An Experimental Investigation of Particle Dampers Under Harmonic Excitation," *Journal of Vibration and Control*, Vol. 4, No. 4, 1998, pp. 361–379. doi:10.1177/107754639800400402

[9] Saeki, M., "Impact Damping with Granular Materials in a Horizontally Vibrating System," *Journal of Sound and Vibration*, Vol. 251, No. 1, 2002, pp. 153–161. doi:10.1006/jsvi.2001.3985

[10] Wu, C. J., Liao, W. H., and Wang, M. Y., "Modeling of Granular Particle Damping Using Multiphase Flow Theory of Gas-Particle," *Journal of Vibration and Acoustics*, Vol. 126, No. 2, 2004, pp. 196–201. doi:10.1115/1.1688763

[11] Fang, X., and Tang, J., "Granular Damping in Forced Vibration: Qualitative and Quantitative Analyses," *Journal of Vibration and Acoustics*, Vol. 128, No. 4, 2006, pp. 489–500.

doi:10.1115/1.2203339
[12] Liu, W., Tomlinson, G. R., and Rongong, J. A., "The Dynamic Characterisation of Disk Geometry Particle Dampers," *Journal of Sound and Vibration*, Vol. 280, Nos. 3–5, 2005, pp. 849–861. doi:10.1016/j.jsv.2003.12.047
[13] Liu, W., Tomlinson, G. R., and Worden, K., "Nonlinearity Study of Particle Dampers," *The International Conference on Noise and Vibration Engineering (ISMA 2002)*, Vol. 1, Leuven, Belgium, The Netherlands, 16–18 Sept. 2002, pp. 495–499.
[14] Rongong, J. A., and Tomlinson, G. R., "Amplitude Dependent Behaviour in the Application of Particle Dampers to Vibrating Structures," 46th AIAA/ASME/ASCE/AHS/ASC Structures, Structural Dynamics, and Materials Conference, AIAA Paper 2005-2327, Austin, TX, 18–21 April 2005.
[15] Witt, B. L., and Kinra, V. K., "Particle Impact Damping in the Horizontal Plane," *47th AIAA/ASME/ASCE/AHS/ASC Structures, Structural Dynamics, and Materials Conference*, Newport, RI, 1–4 May 2006, pp. 7345–7352; also AIAA Paper 2006-2209.
[16] Panossian, H. V., "Nonobstructive Particle Damping (NOPD) Performance Under Compaction Forces," American Society of Mechanical Engineers DE, Vol. 36, *Machinery Dynamics and Element Vibrations: Presented at the 1991 ASME Design Technical Conferences: 13th Biennial Conference on Mechanical Vibration*, edited by T. C. Huang and C. C. Chao, Miami, FL, 1991, pp. 17–20.
[17] Wong, C. X., and Rongong, J. A., "Control of Particle Damper Nonlinearity," *AIAA Journal*, Vol. 47, No. 4, 2009, pp. 953–960. doi:10.2514/1.38795
[18] Flint, E. M., "Experimental Measurements of Particle Damping Effectiveness Under Centrifugal Loads," Fourth National Turbine Engine High Cycle Fatigue Conference, Monterey, CA, 9–11 Feb. 1999.
[19] Flint, E. M., Ruhl, E., and Olson, S. E., "Experimental Centrifuge Testing and Analytical Studies of Particle Damping Behavior," Fifth National Turbine Engine High Cycle Fatigue Conference, Chandler, AZ, 6–9 March 2000.
[20] Meirovitch, L., *Fundamentals of Vibrations*, McGraw–Hill, New York, 2001, p. 109.
[21] Jones, E., Oliphant, T., and Peterson, P., "SciPy: Open Source Scientific Tools for Python," http://www.scipy.org/ [retrieved 4 April 2001].
[22] Wong, C. X., Spencer, A. B., and Rongong, J. A., "Effects of Enclosure Geometry on Particle Damping Performance," 50th AIAA/ASME/ASCE/AHS/ASC Structures, Structural Dynamics, and Materials Conference, AIAA Paper 2009-2689, Palm Springs, CA, 4–7 May 2009.

A. Sinha
Associate Editor